May 2018

Micropillar Arrays Fabricated by Light Induced Self-Writing: An Opportunity for Rapid, Scalable Formation of Hydrophobic Surfaces

Hansheng Li
Syracuse University

Abstract:

Superhydrophobic surfaces naturally exist in plants and animals, which have inspired the development of artificial hydrophobic surfaces. The hydrophobic surfaces have drawn attention in multiple areas in recent years. Multiple approaches were carried out and achieved different levels of hydrophobicity. In this thesis, a series of hydrophobic surface structures have been prepared with a photo-inducted self-writing method and then coated with fluorocarbon compounds. Various fiber heights and different coating methods have been tested for differences and influences in hydrophobicity. Section views using optical microscope showed uniform cone structures fabricated with photo-curing; contact angle measurements that exhibited static contact angles greater than 150 °were achieved. This method is also available for creating translucent samples.

Key Words: Hydrophobic, Self-writing, Micropillar Array

Micropillar Arrays Fabricated by Light Induced Self-Writing: An Opportunity for Rapid, Scalable Formation of Hydrophobic Surfaces

by

Hansheng Li

B.S., Sichuan University, 2014

Thesis
Submitted in partial fulfillment of the requirements for the degree of
Master of Science in *Chemical Engineering*.

Syracuse University
May 2018

Acknowledgements

The author sincerely thanks Dr. Ian Hosein for instructions on conducting research and analyzing the results, and all the help from all co-researchers in the Hosein research group. The author would like to thank the Biomedical and Chemical Engineering Department of Syracuse University, Syracuse Biomaterials Institute (SBI) and the State University of New York College of Environmental Science and Forestry (SUNY-ESF) for providing the labs and instruments.

Table of Contents

1 Introduction

Hydrophobic surfaces contain micro- or nano-scale structures that form roughness, thus making them non-wetting. These surfaces are naturally existing and have drawn attention for a period of time for different purposes,[1–9] and different methods have been used to simulate and produce them. In most cases, when the aquatic contact angle on a surface is greater than 90 °, this surface is considered to be hydrophobic. And when the contact angle reaches or exceeds 150 °, the surface is considered to be superhydrophobic.[10] Rough surfaces are considered more hydrophobic, having greater contact angles.[11,12] There are 3 models describing wetting, Young[13] for ideal flat smooth surfaces, Wenzel[14] and Cassie-Baxter[11] for rough surfaces. The ideal rigid flat surface for Young's model is

$$\gamma_{SG} = \gamma_{SL} + \gamma_{LG} \cos\theta \tag{1}$$

When the surface is not flat, the two roughness models are used. When the wetting is homogeneous, the Wenzel model is used:

$$\cos\theta_W = r \cos\theta_Y \tag{2}$$

Here, r is the surface roughness factor. It equals the ratio of the total surface area and the projected area. When the wetting surface is heterogeneous, the Cassie-Baxter model is used, which is more complex than the Wenzel model,

$$\cos\theta_{CB} = r_f f \cos\theta_Y + f - 1 \tag{3}$$

where θ_Y is the Young contact angle, r_f is the secondary roughness factor,[12] as the secondary structure is filled with liquid and the Wenzel model is being used here[15], and f is the fraction of area wetted of the projected surface. When there is no secondary roughness, r_f=1.

Lotus leaves are naturally rough and are usually chosen as the model to describe superhydrophobicity,[16,17] as shown in Figure 1.

Figure 1 Lotus leaf model

The surface of the lotus leaf contains two levels of roughness, a primary one and a secondary one. The diameter of the primary structures is around 5-10 μm with the height at around 12-18 μm,[18–20] the distance between them at a similar value[18] and the secondary structure is nano-scale, at a diameter of around 30 nm.[19]

Creating hydrophobic/superhydrophobic surfaces has various approaches. On metal surfaces, Li et al.[21] had created hierarchically porous micro/nanostructures on copper using hydro-thermal treatment, and achieved a contact angle of 151.2 °. The same is true on copper surfaces; Shirtcliffe et al. have analyzed the contact angle using Cassie-Baxter equation.[22] On an aluminum surface, Ruiz-Cabello et al.[23] have tested multiple coating performances. To prevent corrosion, Liu et al.[4] electrodeposited Mg–Mn–Ce magnesium plates with cerium nitrate hexahydrate and myristic acid in ethanol and created a series of surfaces with contact angles greater than 155 °. Hermelin et al.[24] have covered zinc electrodes with polypyrrole using an electrochemical method.

On other surfaces, a number of silicon compounds are chosen for hydrophobic systems. Polydimethylsiloxane (PDMS) for example, has low surface tension due to low intermolecular

forces between the chains, and the organic methyl groups surround the Si–O backbone, provides good hydrophobicity[25]. The same reference also mentions that functionalizing PDMS would increase the contact angle. According to Park et al.,[26] coating silica particles with PDMS has achieved a contact angle close to 170 °. Mushroom-like structures produced by Lee et al.[27] have achieved high contact angles with low hysteresis by using silica particles and being treated with plasma. Tropmann et al.[28] have reported fabricating PDMS with micro channels, reaching a hysteresis of 1 °. PDMS/PMMA coating on PDMS by Liu et al[29] and laser rendering by Farshchian et al. also showed good hydrophobicity. PDMS is also useful for being the mold material in fabricating microstructures from lithography.[30,31] Other silanes are used as well.[32] Hydrophobic silica, a simple compound, is also used to manufacture hydrophobic surfaces.[33]

Organic fluorine compounds are also being used in hydrophobic systems because of the electric field of the C–F bond dipole[34] and lower surface energy.[35–37] Perfluorosilane coated by Chemical Vapor Deposition (CVD) on a silicon wafer, reported by Wang et al.[38] achieved a static contact angle of 156 °and hysteresis of 10 °, which shows superhydrophobicity. Perfluoro compounds were also used by other researchers to generate superhydrophobic surfaces. [39–43] Poly(tetrafluoroethylene) (PTFE) is also being researched; Zhan et al.[44] used a laser to fabricate a self-cleaning surface with PTFE; Milionis et al.[45] used PTFE to coat SU-8 pillars and contact angles of over 150 °were acquired.

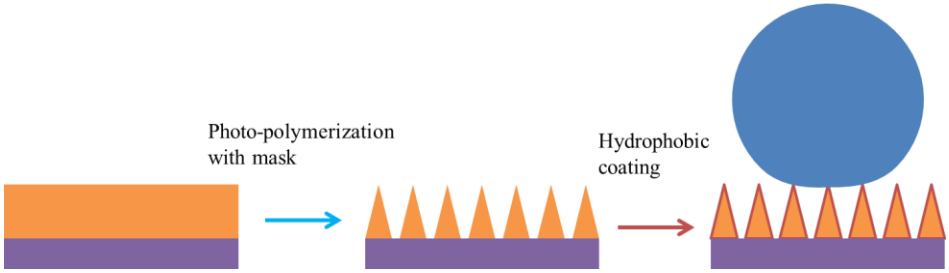

Figure 2 The concept of experiment.

The approach in this article includes two steps, as shown in Figure 2. The first step is the light induced self-writing method, using camphorquinone (CQ) as the main initiator, which has maximum absorbance at the wavelength of 468 nm,[46,47] and is able to generate free-radicals which are favorable for polymerization.[48] To maximize the use of light, a light source with a 470 nm wavelength was chosen. The (4-octyloxyphenyl) phenyliodonium hexafluoroantimonate (OPPI) acts as a cationic initiator.[49] The mechanism[50–52] is shown in Scheme 1. The self-writing pattern is from the mesh mask, with different dimension combinations. The second step is the hydrophobic coating; its main purpose is to generate secondary roughness. The coating process varies for different coating materials.

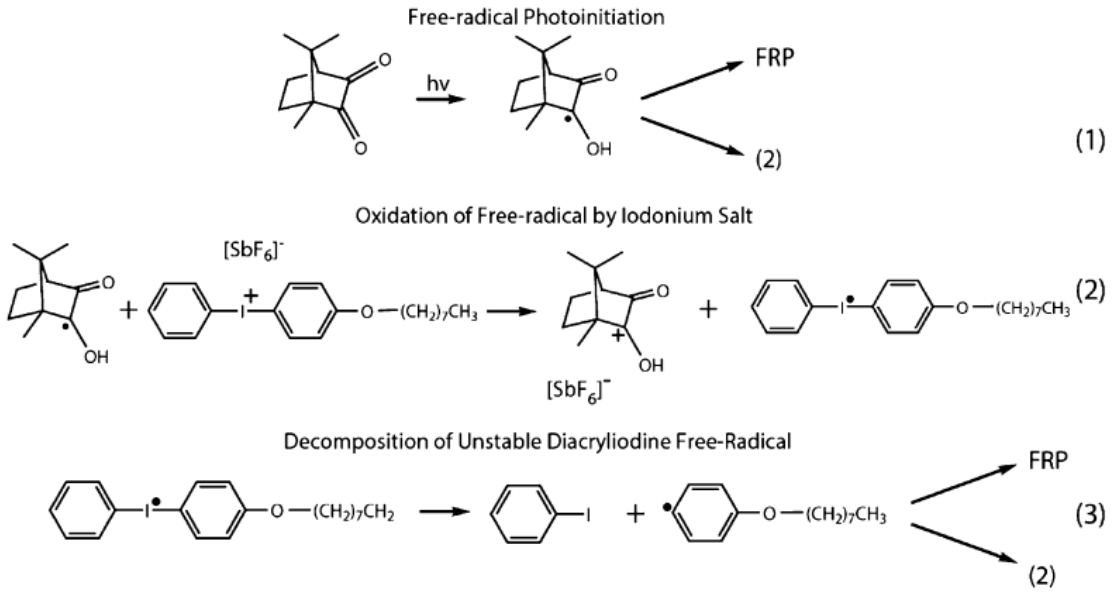

Scheme 1 Reaction mechanism of the initiation

The self-writing method is that when the light beam goes through the mask consisting of specific cylindrical arrays, it diffracts as shown in Figure 3 (a). As the photo-polymerization initiates and is on-going, the polymerized products have a higher refractive index compared to the monomer mixture. Total internal reflection occurs, self-focusing the diffracted light beam (Figure 3 (b) and (c)). The bottom also has a larger diameter than the aperture due to the diffraction. Oxygen

diffusion at the top of the mixture prohibits the growth of the pillars. The thickness of the diffusion layer has correlations with the light intensity and film thickness.[50]

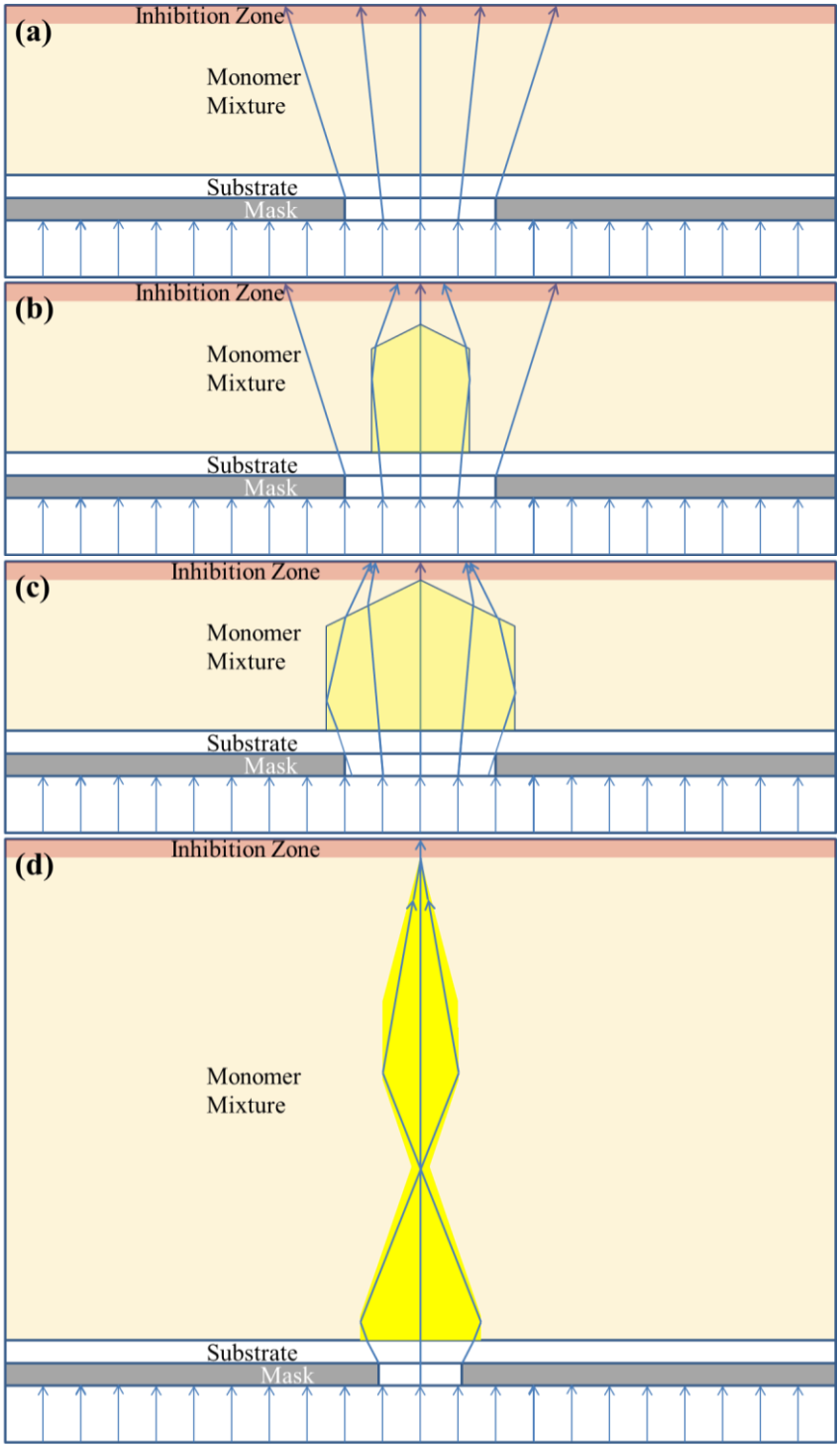

Figure 3 Evolution of the pillar growth

If the film thickness is high enough, it could be derived that the final product would become a "chess piece" (Figure 3 (d)), this is due to the second total reflection happening before the light beams reach the inhibition zone as the "focal point" is lower than the distance from the upper surface of the substrate to the bottom line of the inhibition zone.

2 Experiments and Method

2.1 Material and reagents

Trimethylolpropane triacrylate (TMPTA) was purchased from Sigma-Aldrich and is the basic monomer. The photo-initiating system consists of camphorquinone (CQ) as a free-radical initiator, purchased from Sigma-Aldrich, and (4-octyloxyphenyl) phenyliodonium hexafluoroantimonate (OPPI) as a cationic initiator, obtained from Hampford Research Inc. (Stratford, CT). The hydrophobic coating utilized 1H,1H,2H,2H-perfluorodecanethiol (PFDT) and free flowing polytetrafluoroethylene (PTFE) powder with 1 μm particle size, were both purchased from Sigma-Aldrich. Various solvents were considered for use as the media of the coating mixture. Methanol (MeOH) was acquired from Fisher-Scientific and ethyl alcohol (EtOH) was purchased from Pharmco-Aaper.

2.2 The primary structure

The feedstock solution was prepared with solving CQ and OPPI in TMPTA at room temperature, the weight ratio was 96:2.5:1.5. The mixture was continuously stirred for 24 h without ambient light. As the mixture was ready, it was added to a custom-made cell with a translucent acrylate cover or a 1 mm glass microscope slide as substrate as shown in Figure 4.

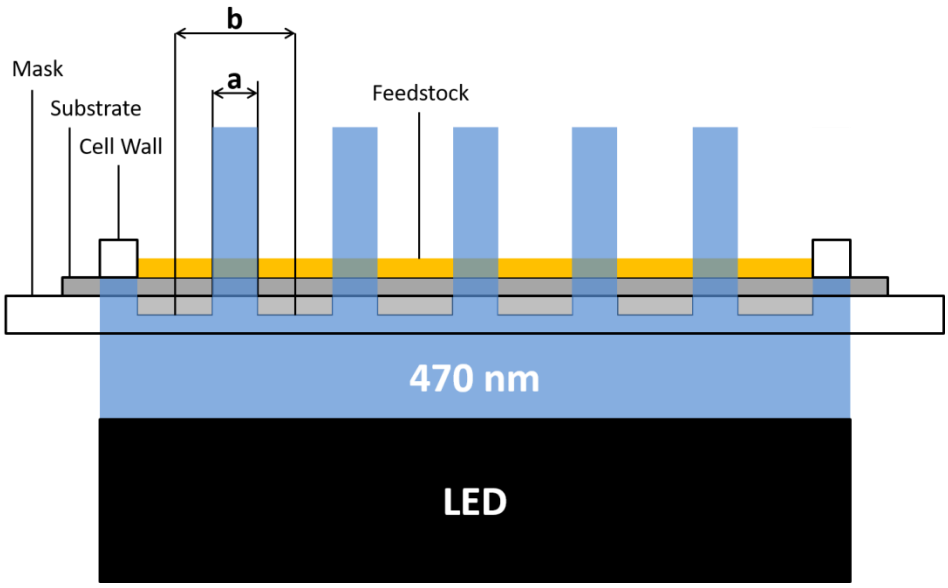

Figure 4 Experiment setup, the spacing of mesh is shown as a/b.

The process of creating the basic structure is shown in Figure 5 A. The thickness of the liquid in the cell was being controlled by varying the volume. The cell was then placed on a transparent mask with printed round mesh, ordered from Photo Sciences Incorporated. The source of light came from a Thorlabs M470L3 LED with a wavelength of 470 nm, coupled with a set of COP4-A collimation adapter, and controlled by a Thorlabs 2100 pulse controller. The controller was therefore remote-controlled by a custom-made program through a USB-COM port.

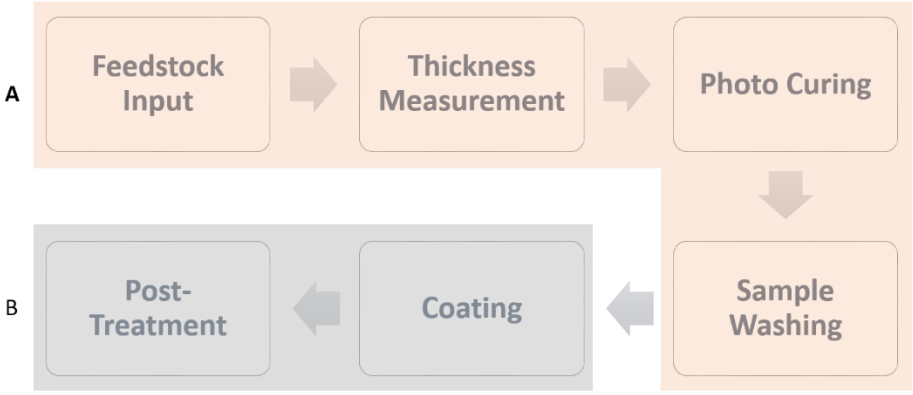

Figure 5 The experiment process

The photo curing process was carried out using a constant light source. The constant mode was set to a specific power calibrated to 10 mW/cm^2. Time was fixed for each specific spacing and power setting. The samples were being soaked with ethanol for 3-5 minute before drying in air.

2.3 The Hydrophobic Coating

The entire hydrophobic coating process is shown in Figure 5 B. The coating method varies depends on the coating mixture.

The hydrophobic coating mixture 1 (HPCM-1) was prepared by solving CQ and PFDT in a specified solvent with a weight ratio of 1:1:98. The coating mixture was continuously stirred for 24 h with no ambient light before utilizing. The coating procedure was to drop different volume of the coating fluid on the surface of the basic structures and cover with a reversed cell to reduce the evaporation of the solvent. The reaction was processed using a similar set-up to that shown in Figure 4, except that the mask was replaced with a glass microscope slide, with the LED power maintained at 10 mW/cm^2 and facing upright for the thiol-ene reaction, the simplified reaction is shown in Scheme 2. After washing with methanol, the samples were let dry in a fume hood.

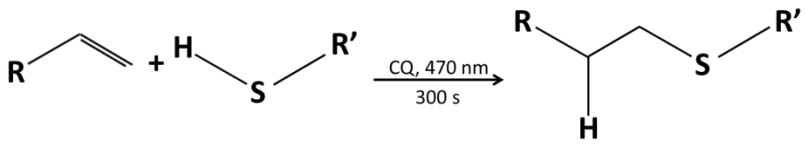

Scheme 2 The thiol-ene reaction for chemical coating. Here, R refers to the poly-TMPTA and R' refers to $(CH_2)_2(CF_2)_7CF_3$.

The hydrophobic coating mixture 2 (HPCM-2) was prepared mixing PTFE powder and ethanol, at a weight fraction of 5 %. The mixture was being processed with vortex mixer and ultrasonic bath for 30 minutes before use for better mixing. The mixture was added to a spray gun and

sprayed on the samples prepared at 40 psi nitrogen or drop on the samples. The samples were let dry in fume hood.

2.4 Contact Angle Measurement

The contact angle measurements were carried out using a Ramé-Hart 250 F1 contact angle goniometer. The DROPimage Advanced controlling software automatically calculates the contact angles from the images captured via the camera lens, fitting the tangent line. The data of each sample for analysis were collected 10 times within 1 second. The errors in analysis are standard deviations. ImageJ software developed by the National Institutes of Health (NIH) was also used in analyzing the images, with the contact angle plug-in developed by Marco Brugnara.

2.5 Microscopy

The microscope images were captured using a Zeiss Axioscope A1, equipped with Axiocam 105 color camera and monitored by Zeiss Efficient Navigation (ZEN) Lite software. The microstructure dimensions were measured using ZEN Lite software. The zoom-in photographs were captured using a Venus USB 2.0 Digital Microscope with manual zooming and focusing. The same digital microscope was also used to film a few video clips of the droplet and the sample.

2.6 Scanning Electron Microscopy (SEM)

The SEM images were obtained with a JEOL JSM-IT100 scanning electron microscope, with tungsten/lanthanum hexaboride (W/LaB_6) filament-cathode combination. The samples were sputter-coated with gold-palladium at 45 mV for 60 s, and the acceleration voltage was set at 10.0 kV and 7.0 kV.

3 Results and Discussion

3.1 The Structure

The structures generated by the first process are uniform multi-fiber/pillar standing structures, with a slab forming on the substrate. This was formed by the initiation of CQ and OPPI under the specific wavelength of 470 nm, a blueish visible light. This mechanism for the entire reaction is free-radical and was described by Chen et al..[50] The roughness (r) and area fraction (f) are defined as[53]

$$r = 1 + \pi\left(\frac{d\,H}{b^2}\right) \tag{4}$$

$$f = \left(\frac{d}{b}\right)^2 \tag{5}$$

where b is the pitch, or the spacing, d is the cylindrical diameter and H is the height when the structure is cylindrical.

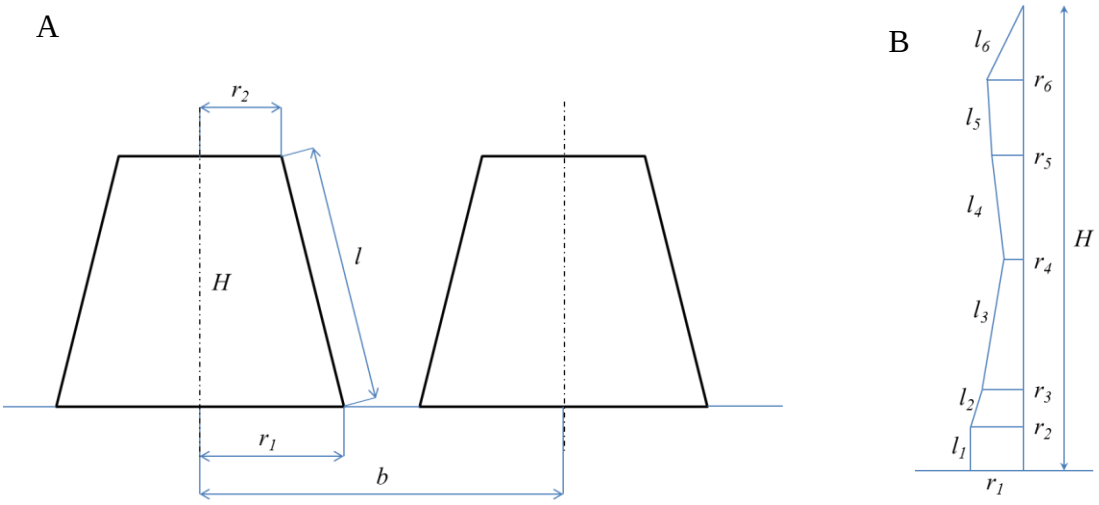

Figure 6 Section views of shapes. (a) Conical frustum; (b) Irregular (chess piece);

Similarly, when the structure has the shape of a conical frustum (Figure 6 A), first calculate the surface area:

$$S_P = \pi(r_1 + r_2)l \tag{6}$$

S_P here denotes the surface area of a single pillar structure, and l is leg length of the right trapezoid.

For irregular shapes (Figure 6 B and Figure 3 (d)),

$$S_P = \pi \sum_1^n (r_i + r_{i+1})l_i + f(r) \tag{7}$$

$$f(r) = \begin{cases} \pi r_{n+1} l_{n+1}, & conical\ top; \\ \pi r_{n+1}^2, & flat\ top; \end{cases} \tag{8}$$

Here, r_i is the radius of the solid of revolution, while l_i is the length of the leg of the right trapezoid. Thus,

$$r = 1 + \frac{S_P - \pi r_1^2}{b^2} \tag{9}$$

$$S_E = S_P - S_{Non} \tag{10}$$

$$f = \frac{S_E}{b^2} \tag{11}$$

S_E is the area of effective contact surface; it equals the value of subtracting the non-contacted surface areas (S_{Non}) from S_p and f is used to calculate the Cassie-Baxter contact angle using Eq. (3). The microscopic images were used to determine S_{Non} together with the measurements, and it was calculated using similar methods to those in Eq. (7) and (8).

The uniform spacing is designated by the mask being used (Figure 7 A to D) and the height is strongly related to the initial thickness of the feedstock film.[50] The single structure is cone-

shaped, with a larger diameter at the bottom and a tip on the top (Figure 7 E). Changes in height also alter the shape (Figure 7 F), affecting *r*, and in this figure, when H is significantly lower, r is also lower. The slab at bottom was formed either from the diffraction of light initiating the reaction or from the diffusion of initiated free-radicals proceeding reaction between structures.

Flaws in structure (Figure 7 A) are likely to be formed by the unevenness of the plastic substrate being used. Glass is considered to have better evenness and better transmittance than the thinner plastic substrate and when glass is being used as the substrate (Figure 7 C), the uniformity is increased, at the cost of sample adhesion to substrate. The samples on glass substrates are likely to flip and twist over time (Figure 7 D) which changes the tip spacing and uniformity of the surface structures and therefore prevents the samples from having a further use (i.e. the coating procedure). The twist is likely to be caused by internal stress on the surface of slab, which is formed by the residue of TMTPA. Plastic substrates tend to adhere with the sample from the poly(methyl methacrylate) (PMMA) from the cross-linking of their residues on the interface.[54] Reducing the thickness of the slab or eliminating it would be necessary for processing on glass substrates. However, due to the refractive index it is less likely to prevent the slab from forming on glass.

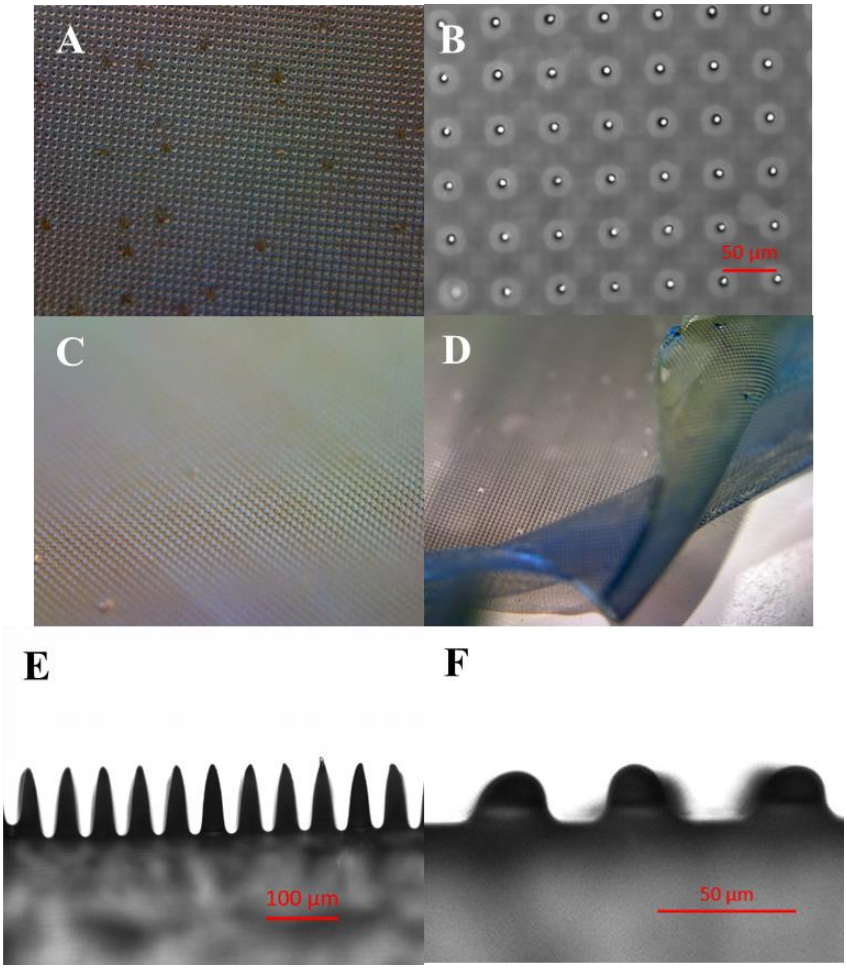

Figure 7 A: Zoom-in photograph of a sample with 10/50 spacing on a plastic substrate; B: Microscope image of the same sample; C-D: Sample on a glass substrate with 10/50 spacing; E: Sectioned view of the 10/50 sample with an initial thickness of 310 µm; F: Sectioned view of a sample with 10/50 spacing and 270 µm initial thickness.

Figure 8 A is a column chart showing the contact angles of samples with basic structure and no coating, with respective goniometer images shown as Figure 8 B to E. The curve in Figure 8 B is the edge of the sample in the background. Generally, the hydrophobicity increases as the surface roughness increases. One exception is the sample with 280 µm initial thickness. Due to the limitations of the goniometer and sample cutting, the background is always shown in the images, thus it leads to inaccurate measurements. The 280 µm sample itself may have unevenness or a damaged structure that accounts for the lower contact angle.

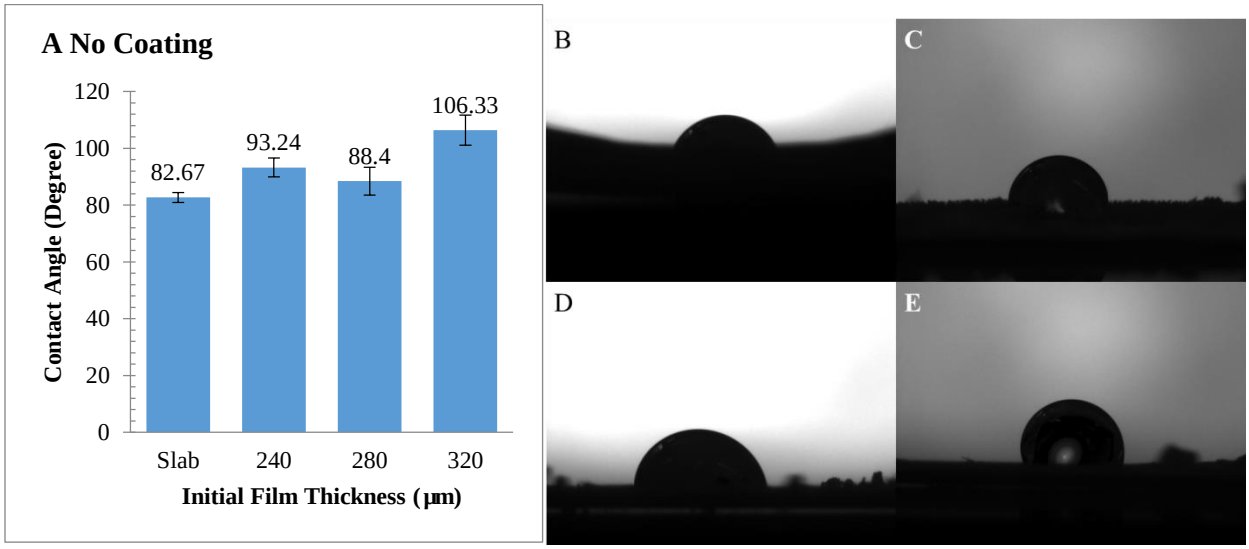

Figure 8 Non-coated samples with different height, Spacing 10/50. A: Contact angles; B-E: Images captured with goniometer for Contact Angle Measurement, Slab, initial thickness of 240 µm, 280 µm, and 320 µm, respectively.

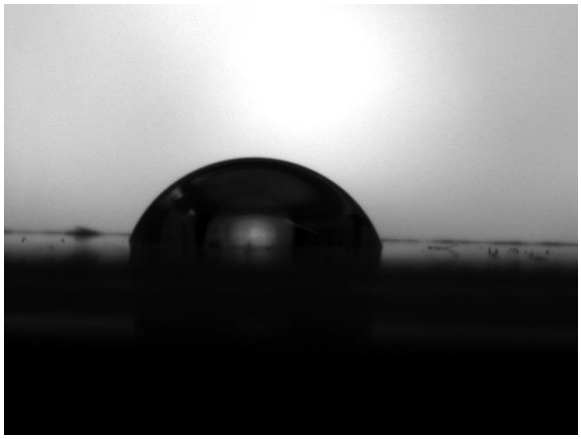

Figure 9 Clean substrate with an average contact angle of 64.82 °

According to Figure 9, a pure PMMA substrate has an average contact angle of 64.82 °. For the sample as shown in Figure 8 D, which has a very close value to the bare substrate, it is possible that the area for measurement had insufficient effective structure left for some reason, and the surface was close to pure flat PMMA.

3.2 The Coating

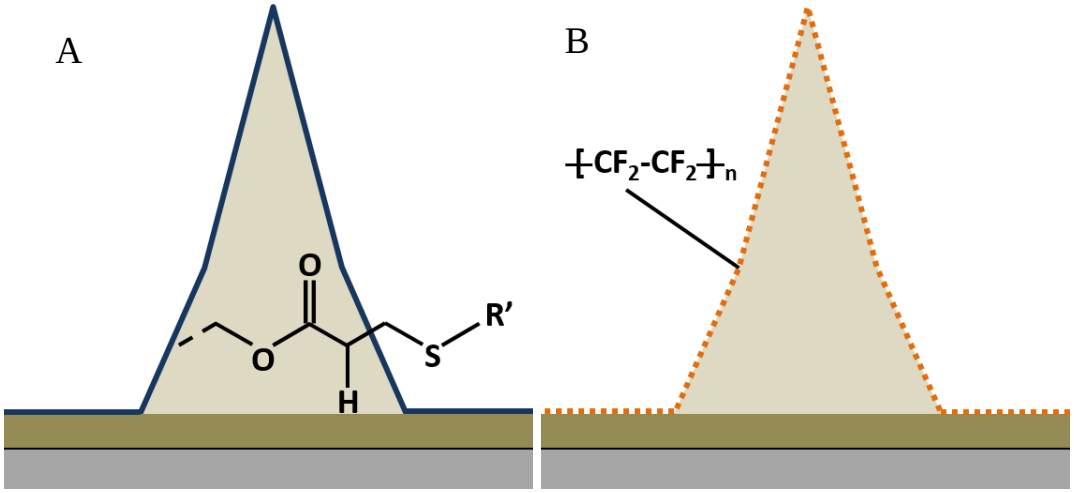

Figure 10 Two different types of coating composition: A: PFDT coating, chemically bonded; B: PTFE coating, physically adhered; Bottom layer: substrate; Dark layer: Slab/gel; Light layer: micro-pillar/primary structure.

Three coating procedures were carried out for testing. The PFDT coating reaction, the thiol-ene reaction mechanism has been described by Crivello et al..[55] Since the photo-polymerization reaction of the basic structure is like cross-linking of TMPTA, the initial guess was that some of the C=C bonds from poly(TMPTA) remained as residues after the initial photo-curing, and thus could have further reactions with –SH function groups that existed in the HPCM-1 solution, with CQ as the initiator. The hydrophobic part, the fluorocarbon chain, is chemically attached to the surface of the structure, as shown in Figure 10 A.

Figure 11 A shows the hydrophobic performance of 10/50 samples after two times of coating. Washing and drying procedure were carried out between the two coating procedures to clean out the excess fluorocarbon chains covering the surface. The mixture was added to fill the space between primary structures, and the reaction was desired to occur on the surface of the primary structure. When the lights came from below, most of them would go through the slab on the bottom and the reaction occurred there. The cone pillars would restrict the light coming out on

their surface due to the refraction index so the reaction was limited on desired surfaces; also, excess light absorbed and the presence of oxygen[56] could make two PFDT molecules link. The –SH group could be initiated by the free radicals generated by CQ in the presence of light and form –S–S– bonds ; and when the light source was on top and facing down, the unfavorable linking reaction would occur on the surface of the mixture and the side product would accumulate between pillars as the solvent evaporated.

The slab prepared for contact angle measurement formed cracks after coating due to internal stress, and this restricted the hydrophobicity (measured contact angle of 74.7 °) of this specific sample. The sample with an initial film thickness of 280 μm had achieved an average contact angle of 129.93 °, as shown in Figure 11 B, followed by the one with a 320 μm initial film thickness. It is possible that the solvent evaporates before the tip has enough PFDT molecules attached to the surface. The one with 240 μm initial film thickness achieved a lower contact angle, which was due to a different shape without a "sharp" tip, resembling a bump. The one labeled as a slab was photo-cured without a textured mask and the surface was flat, which led to poor performance compared to the ones with structures. Similar to the one with a "bump" surface, the flatness greatly reduced the performance of PFDT.

The PFDT coating was tested for more times as shown in Figure 11 C. Coating samples at 3 times show poor hydrophobicity comparing to the twice-coated ones, and the fourth coating had no better results than the third one. It is assumed that the surface residues had been consumed after the second coating and starting from the third coating, the excess PFDT could no longer react with the surface. The molecules started linking themselves as described above, and the side products possibly either got stuck between the existing secondary structures, filling the gaps and creating uneven roughness, or they would accumulate at the bottom surface.

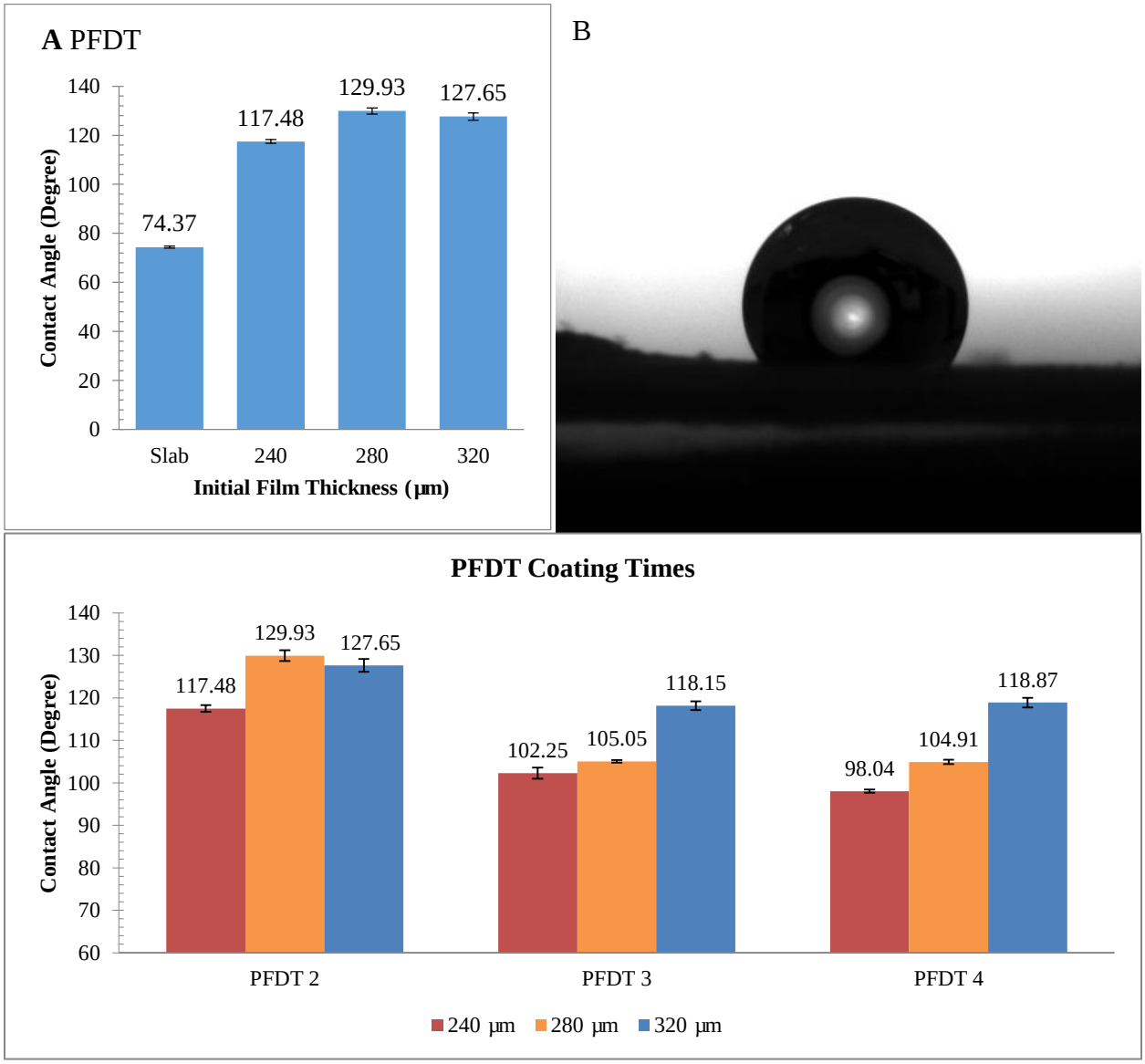

Figure 11 Contact angles of samples. A: PFDT coating twice; B: Twice-coated sample with 280 µm initial thickness; C: Coating of PFDT, 2-4 times.

The coating of PTFE is intended to let the particles physically attached to the surface, as shown in Figure 10 B. Figure 12 A shows the results from dripping the samples with a 5% wt. PTFE mixture (HPCM-2). Compared with the results shown in Figure 11 A, the 280 µm and 320 µm coatings showed less hydrophobicity, with smaller contact angles. The one with highest flatness, the slab one, had a very similar contact angle to the highest one in the group, the 280 µm one.

Since the HPCM-2 was dripped onto the surfaces, the flatness of the slab let the particles distribute more evenly on the surface; with the help of the roughness created by PTFE particles, the hydrophobicity is increased. And for the samples with structures, it was more likely that the particles were mainly precipitated onto the bottom, with fewer particles on the tips of structures. The sample with 240 μm initial thickness had the smallest contact angle among all the samples in this group. The reason for this goes back to the shape –the "bumps" had very low heights, and the particles accumulated between the short structures and increase the flatness, resulting in a lower *r*. The particles intended to create secondary roughness were unable to achieve good distribution with this method.

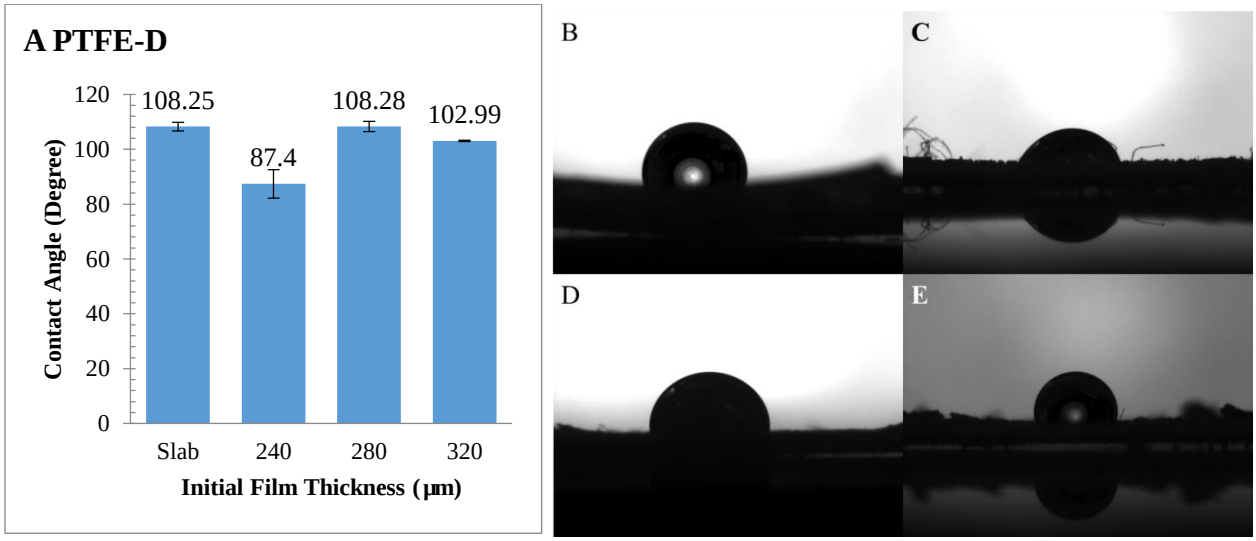

Figure 12 Samples coated with dripping PTFE. A: The contact angles; B-E: Goniometer images for processing, slab, 240 μm, 280 μm, and 320 μm initial thicknesses, respectively.

Another coating method, spray coating, was considered after the ineffectiveness of drip coating. The contact angle comparison is shown in Figure 13. As can be seen, spray coating is better in all initial thicknesses. A brief result is shown in Figure 14. In Figure 14 A and B, the sample was not coated, and the hydrophobicity is poor. After coating, comparing Figure 14 A and C, the

surfaces are highly similar; the white line on the coated one is the accumulation of PTFE particles. The droplet in Figure 14 D has a significantly higher contact angle than the one shown in Figure 14 B, indicating that the hydrophobicity of the surface has increased.

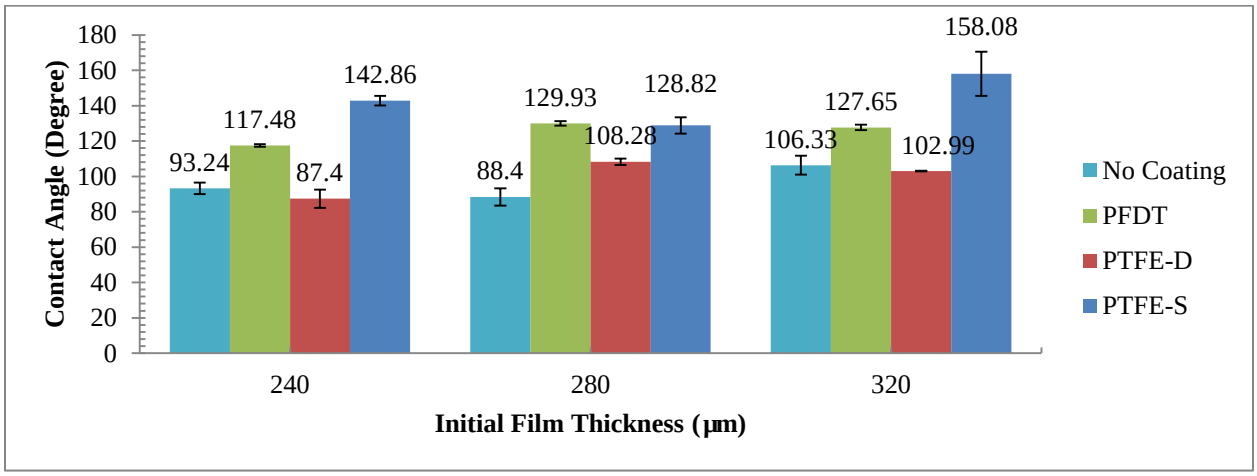

Figure 13 Contact angle comparison, PTFE-S refers to PTFE spray coating, and PTFE-D refers to drip coating.

Table 1 Linear Regression of Height *H* versus Thickness *T* for 10/50 Samples

	Thickness *T* (µm)	Structural Height *H* (µm)
Data Points	241	36.6769
	262	55.021
	281	49.59908
	304	103.2395
	320	115.1505
Linear Regression (1)	H=1.0319 T - 218.645, R^2=0.834115	
Linear Regression (2)	H=1.02784 T - 212.071, R^2=0.994045 (281 Excluded)	

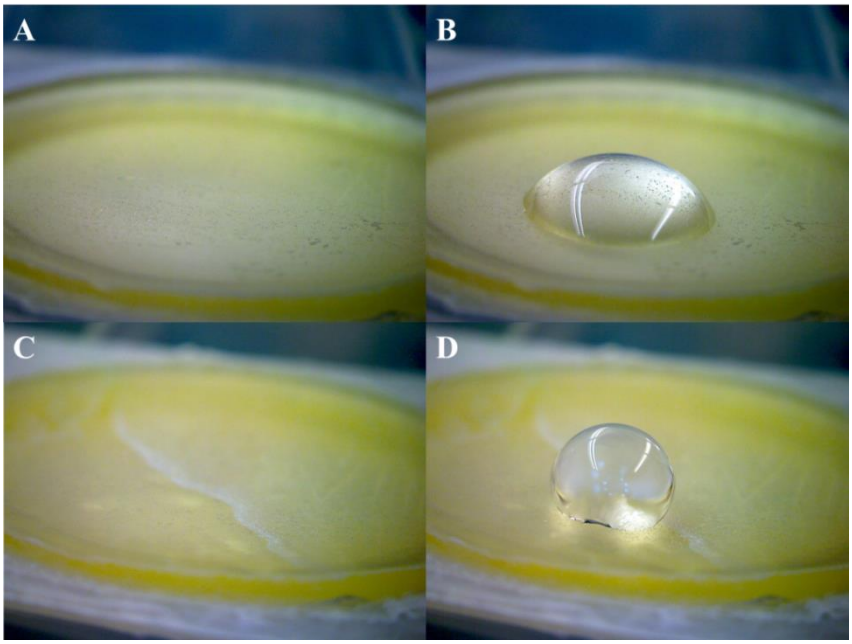

Figure 14 Slab before and after spray coating. A: Before coating; B: Droplet on non-coated surface; C: After coating; D: Droplet on coated surface.

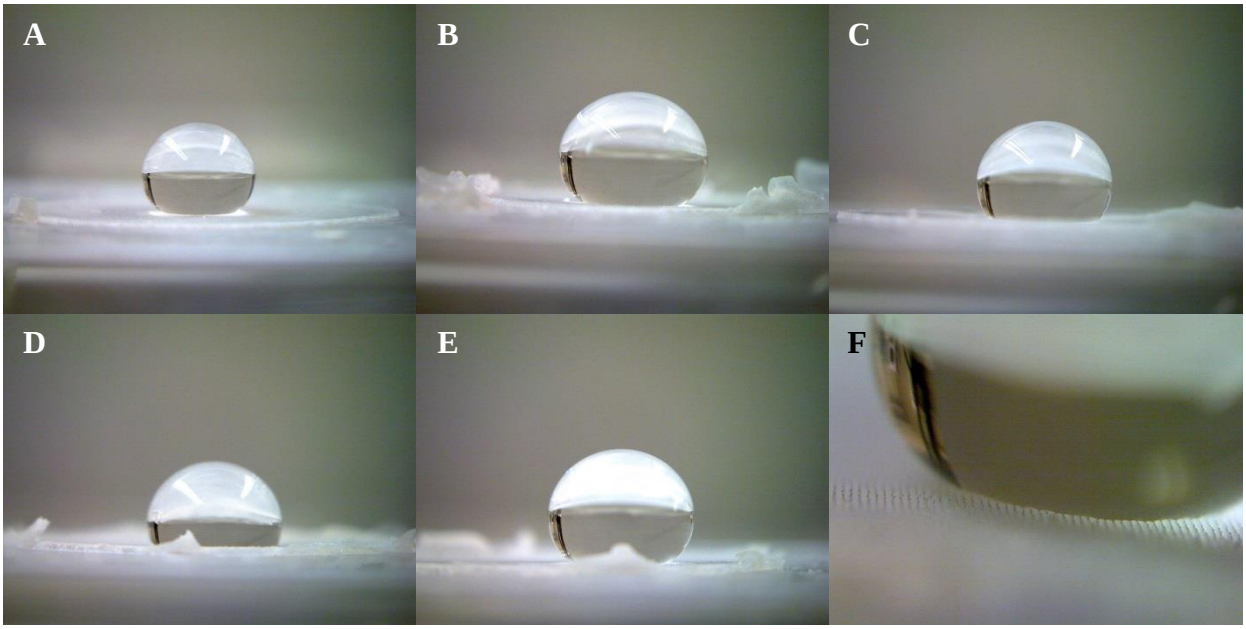

Figure 15 Droplets on five 10/50 spacing samples with various initial film thickness. A-E: Initial thicknesses from 240 μm to 320 μm, 20 μm common difference; F: Zoom-in of the 320 μm sample interface.

Figure 15 shows the 10/50 samples' hydrophobicity briefly. The contact angles are greater than 90 °. The one in Figure 15 C is of the same initial film thickness as the ones with the largest contact angles when coating with PFDT and dripping PTFE. However its height was found to be irregular as shown in Table 1 two linear regressions were carried out. Figure 15 F shows the interface of the droplet and the primary structure, and demonstrates the pillars that were supporting the droplet.

The reason hydrophobicity increased is that the PTFE particles used were fine ones with a particle size of 1 µm. As the particles were sprayed onto the sample, they were more evenly distributed across the surface of structures when the solvent in the suspension evaporated rather than accumulating on the slab. On a lower scale, this created a higher r on the contact surfaces.

3.3 Spacing and Contact Area

Masks with various mesh spacing were available, and the results were mixed. The masks being tested were 5/50, 10/100, 40/100, 40/200, 40/400, 80/200, and 80/400. The masks were divided into groups. All the samples were spray-coated except the 5/50 samples are shown in Figure 16.

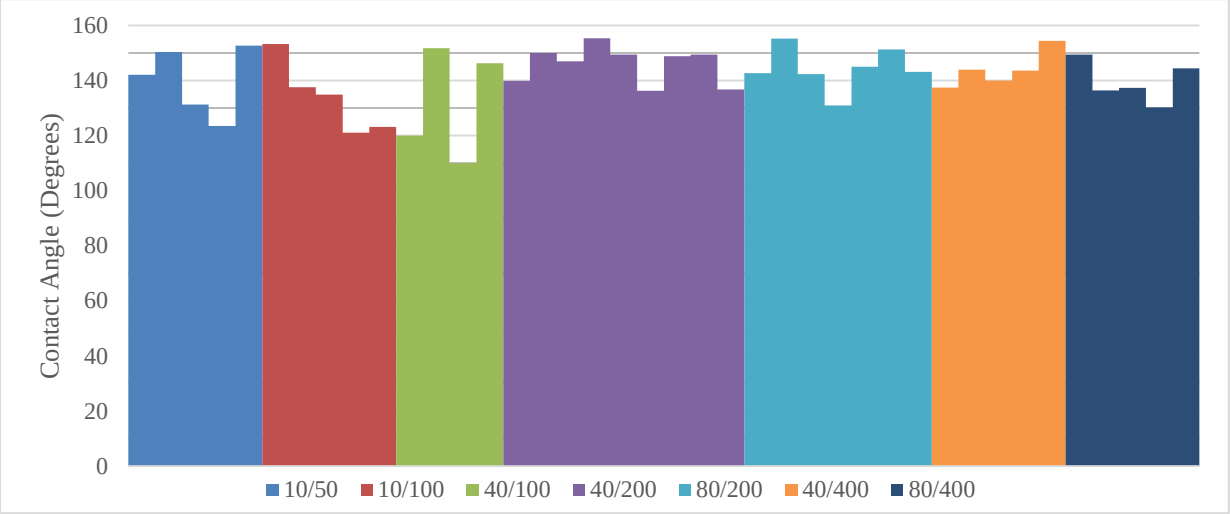

Figure 16 Contact angle values of all PTFE spray coated samples, with increasing sample film thickness for each group.

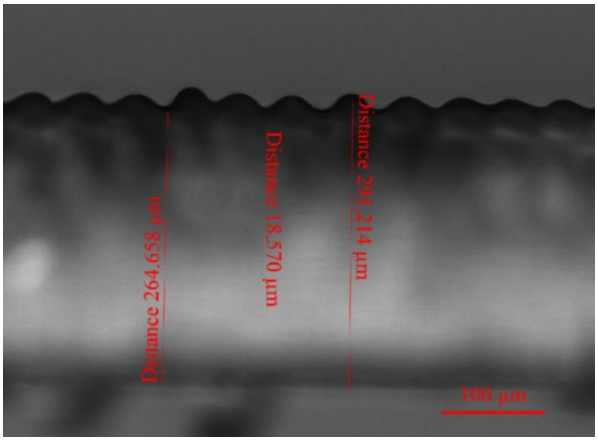

Figure 17 Section view of a 5/50 sample with an initial thickness of 600 µm.

The 5/50 samples showed very poor results due to the shape of the structure, in which the initial thickness was restricted by both oxygen inhibition and the value of the aperture. Compared with the 10/50 samples, the holes had an aperture diameter of 5 µm, the light would have stronger diffraction effect; it photo-polymerized most of the monomer molecules in the lower section, leaving small bumps on top with low H values, as shown in Figure 17.

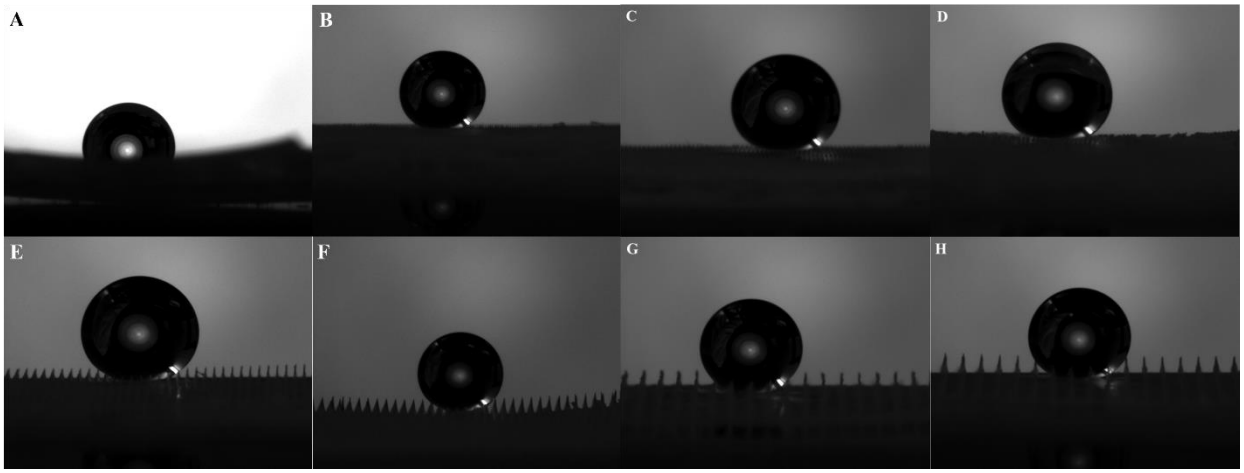

Figure 18 Highest Contact Angles Achieved with PTFE Spray Coating. A: Slab (Basis value, θ=108.25 °); B: 10/50; C: 10/100; D: 40/100; E: 40/200; F: 80/200; G: 40/400; H: 80/400.

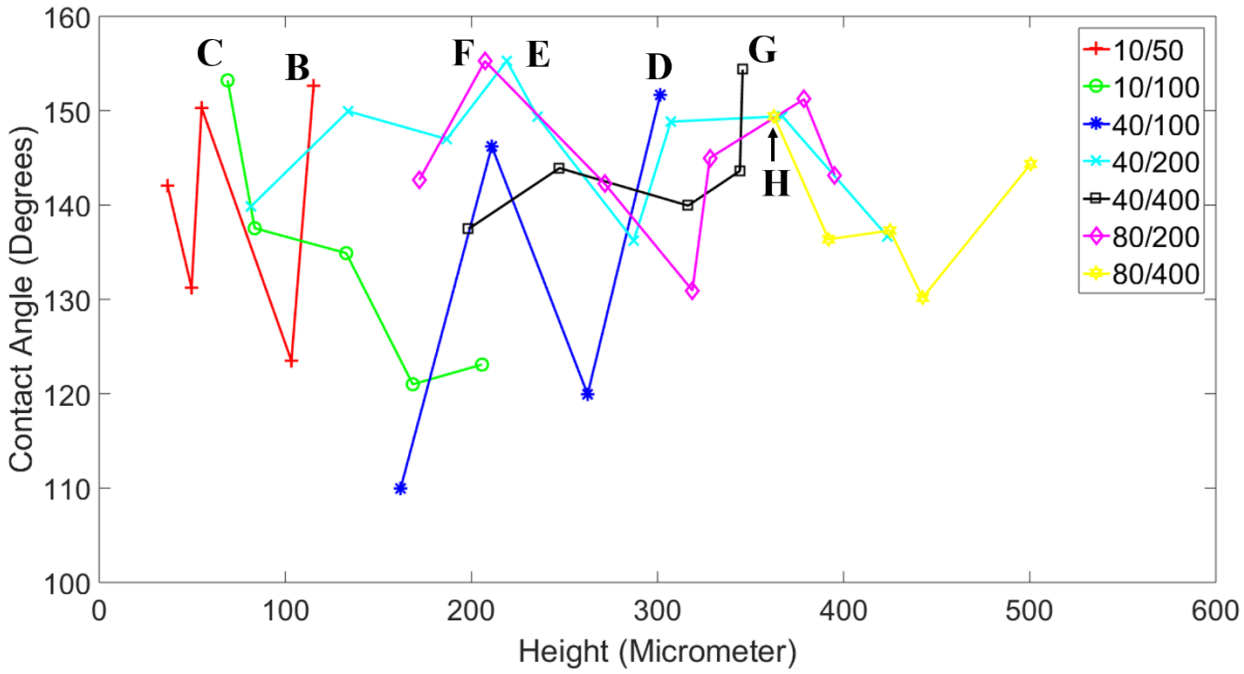

Figure 19 Contact Angle versus Structural Height (*H*), also the caption letters are the corresponding pictures in Figure 18.

The best results from the goniometer are shown in Figure 18, and Figure 19 shows the contact angle values versus the mean actual sample structure height value (*H*) included in Figure 16. The 50 μm samples formed a "W"-shape plot, and the structural heights did not follow the film thickness. The former phenomenon indicates that the two with lower values may have had an undesirable tip surface for higher contact angle while the latter one is possibly due to the high viscosity in which the thickness equilibrium was formed after measurement or a loading process that tilted and in which the equilibrium had not been reached before the reaction started.

As for the distance at 100 μm, 10/100 samples have different hydrophobicity compared with 40/100 samples. The desired contact surfaces are shown in Figure 20 A-B. The 10/100 samples with greater initial thickness tended to bend on the tip and generate more heterogeneity and the contact angles decreased. This may have been due to the path of the light being affected by heterogeneity in the film or disturbance during the washing process, as when thickness increases,

the height increases, the top of the structure has a small diameter and the strength is weak, even with a longer curing time than all other groups; thus the strength is inferior to the others. The tendency is to decrease with the increase of height, which can be seen in the figure. The 40/100 samples have a larger aperture diameter compared with the distance, allowing the free radical diffuse into the covered area more easily and started forming a "bridge". If the film thickness is greater, a slab of polymers is formed, then the layer cracks due to the internal stress and breaks the uniformity of the primary structure when the initial thickness is greater than 450 μm. The measurement of both the 40/100 300 μm and 400 μm were affected by the image background and may not be accurate, as in Figure 19 there are two significant lower value points, as the samples are suffering from the heterogeneity of the surfaces. And despite the fact that there were two samples with very high contact angles, the droplets did not roll well as the other samples with similar contact angles, indicating larger hysteresis.

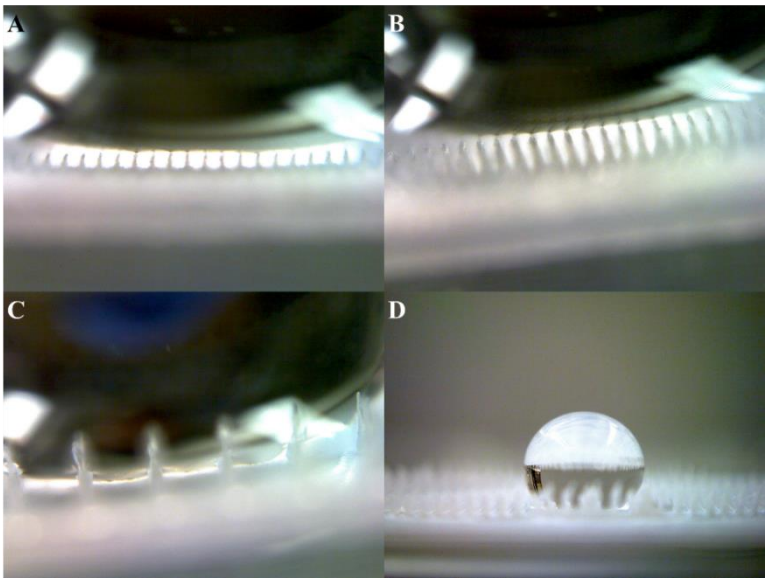

Figure 20 A and B: Contact Surfaces of two 100 Samples. A: 10/100 sample; B: 40/100 sample; C and D: Water Interaction with Structures for 400-Spacing Samples. C: 80/400 with partial immerse; D: 40/400 with full immerse.

For the spacing value of 200, the results show good hydrophobicity for both 40/200 and 80/200

sub-groups. The contact angles of both sub-groups results are also shown in Figure 16. The spray coating of PTFE proved to be very effective for the 200 group. In Figure 21 A, the sample is uncoated and the hydrophobicity is not good, as shown in Figure 21 B. After coating, the sample primary structures remain visible in Figure 21 C; the contact angle has increased compared to Figure 21 B and D. Figure 21 E is a 40/200 sample interacting with a droplet, and the "support" of the tip is visible. A view from a lower angle is available as seen in Figure 21 F, which is an 80/200 sample being shown. The droplet can be seen "floating" above the slab at the bottom, supported by the primary structures. This image is actually a screenshot from a video clip showing the droplet and the sample as the droplet was unstable at the position in the figure.

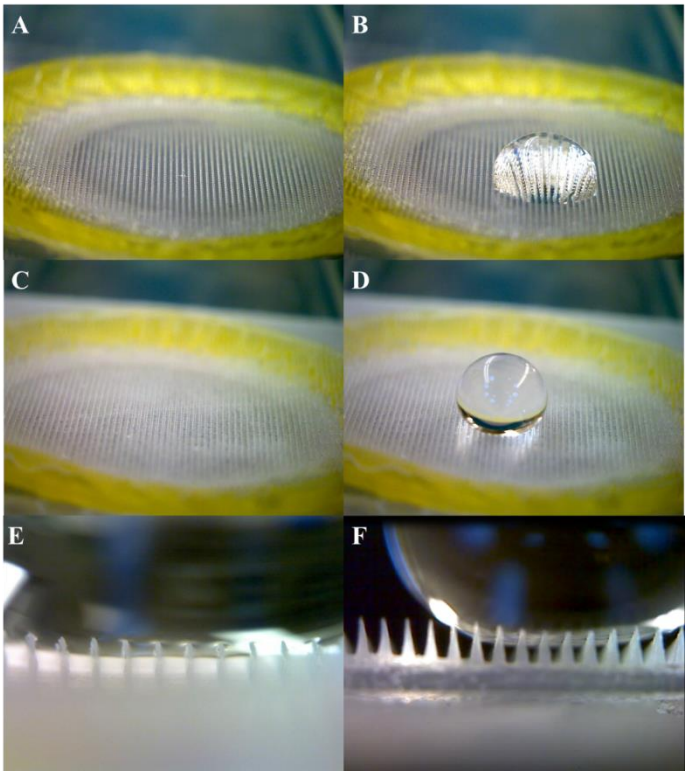

Figure 21 A-D: 80-200 Sample; A: The pre-coated sample; B: Droplet on the pre-coated sample; C: Sample after coating; D: Droplets on coated sample; E: Zoom-in view of droplet interact with microstructures, 40/200 spacing; F: Side view of a moving droplet and structures, 80/200 spacing.

For the distance value of 400 μm, the distance is considered too far for free-radicals to diffuse and react, also for the light to have enough diffraction. It is also considered that the primary structures are not dense enough (b is too large for droplets) or long enough to provide enough support to the droplet. The surface tension could not hold the sphere shape and the water touched the bottom, and the pillars are seemingly penetrating into the droplets in Figure 20 C and D, thus showing a transition state from Cassie-Baxter state to Wenzel state (touching the slab or substrate) a macro "mushroom" state[57] or a Wenzel state. The high contact angle values of droplets are due to the surface roughness provided by PTFE particles on the substrate surfaces. The droplets would not roll even when the contact angle was high. Their contact angle could also be seen in Figure 16. In order to not form the Wenzel state, a higher structural height value H may allow enough clearance for the droplet to be supported by the structure, or a different tip shape would allow more particles to adhere to the tip, creating higher secondary roughness to alter the hydrophobicity of the 400-group samples.

3.4 Shape, Surface and Droplet Analysis

Though the profiles of the pillars could be acquired from the section views, the exact shapes of the structures remain unknown. The equations in Section 3.1 are based on solids of revolution. To verify this, exact three-dimensional views are necessary. Also, the performance of the coating was shown in the previous section, and the exact coating surface morphology and topography are as yet unknown in this research. The following characterization and modeling were carried out to provide sufficient support for the analysis.

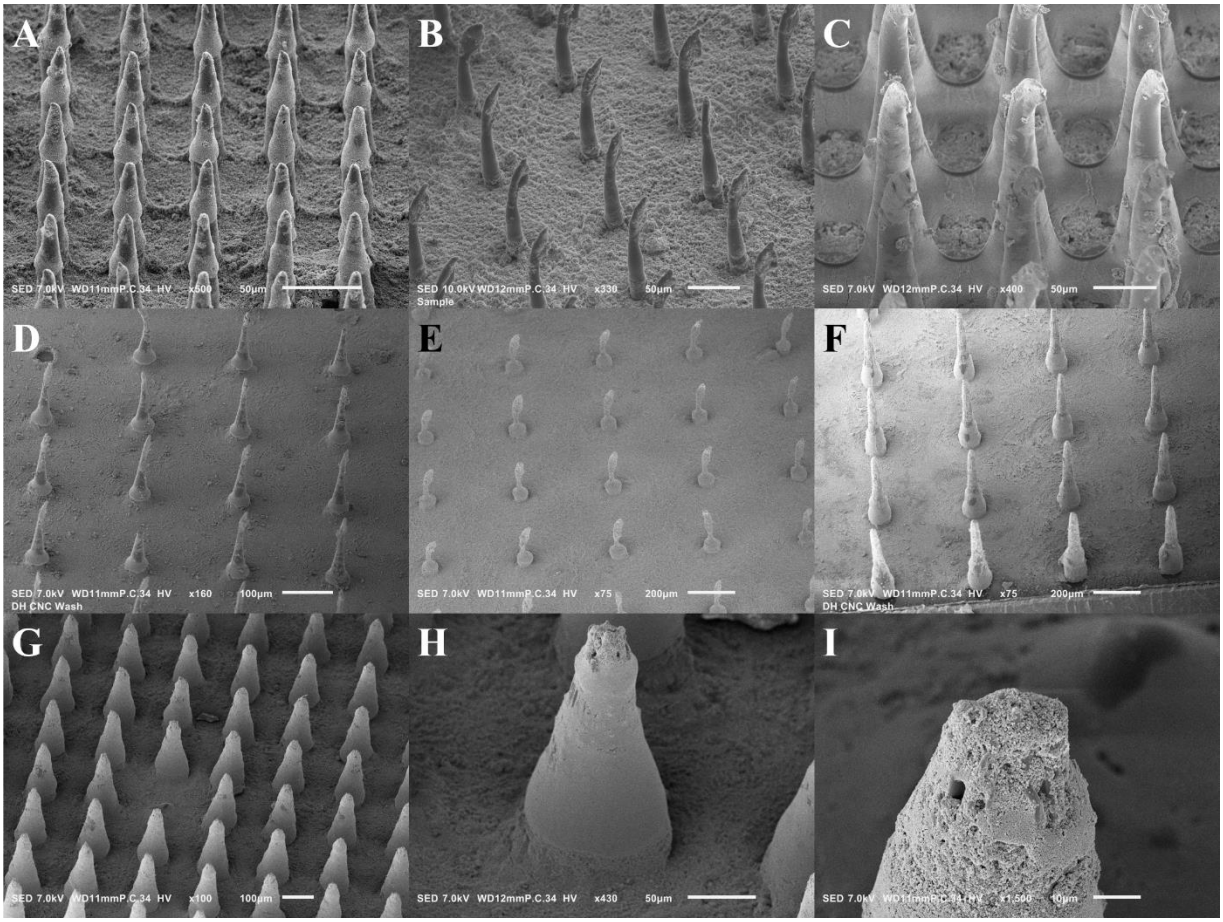

Figure 22 Scanning Electron Microscope (SEM) images. Array View (A-G): A: 10/50; B: 10/100; C: 40/100; D: 40/200; E: 40/400; F: 80/400; G: 80/200; H: Single Structure of 80/200; I: Tip of Structure, 80/200.

The scanning electron microscope (SEM) was being used to analyze the shape of structures and the surface of structures. Figure 22 A to G show the arrays of structures, formed by the self-writing process. The array density is based on the photo mask, and the base radii of pillars are normally larger than the aperture diameters of the masks, due to the dispersion of light and free radicals. A lower aperture/spacing ratio is more favorable to forming “chess piece” pillars. Figure 22 H shows the exact shape of a single pillar, which shape could be used to verify the approximation model. Figure 22 I is a higher magnification image of (H), showing the PTFE particles are effectively coated onto the surface (the white areas with particles) and the non-

coated area is minimal (darker area slightly shown). This has also proved that with an appropriate structural shape, spray-coating of PTFE particles would be a fast and effective way to generate a coating layer.

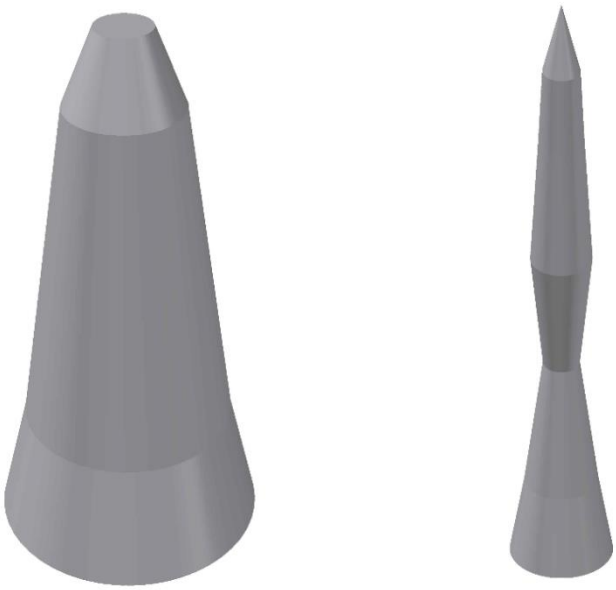

Figure 23 3D Models Based on Approximation Data. A: 80/200; B: 40/400.

Two examples of approximation models for calculation of *f* and *r* are shown in Figure 23. These models were generated using Autodesk® AutoCAD 2015 software. Multiple r_i and l_i values were measured with Zeiss ZEN Lite and put in tables for approximate calculation of SP, then equations (7) to (11) were used to get *f* and *r*.

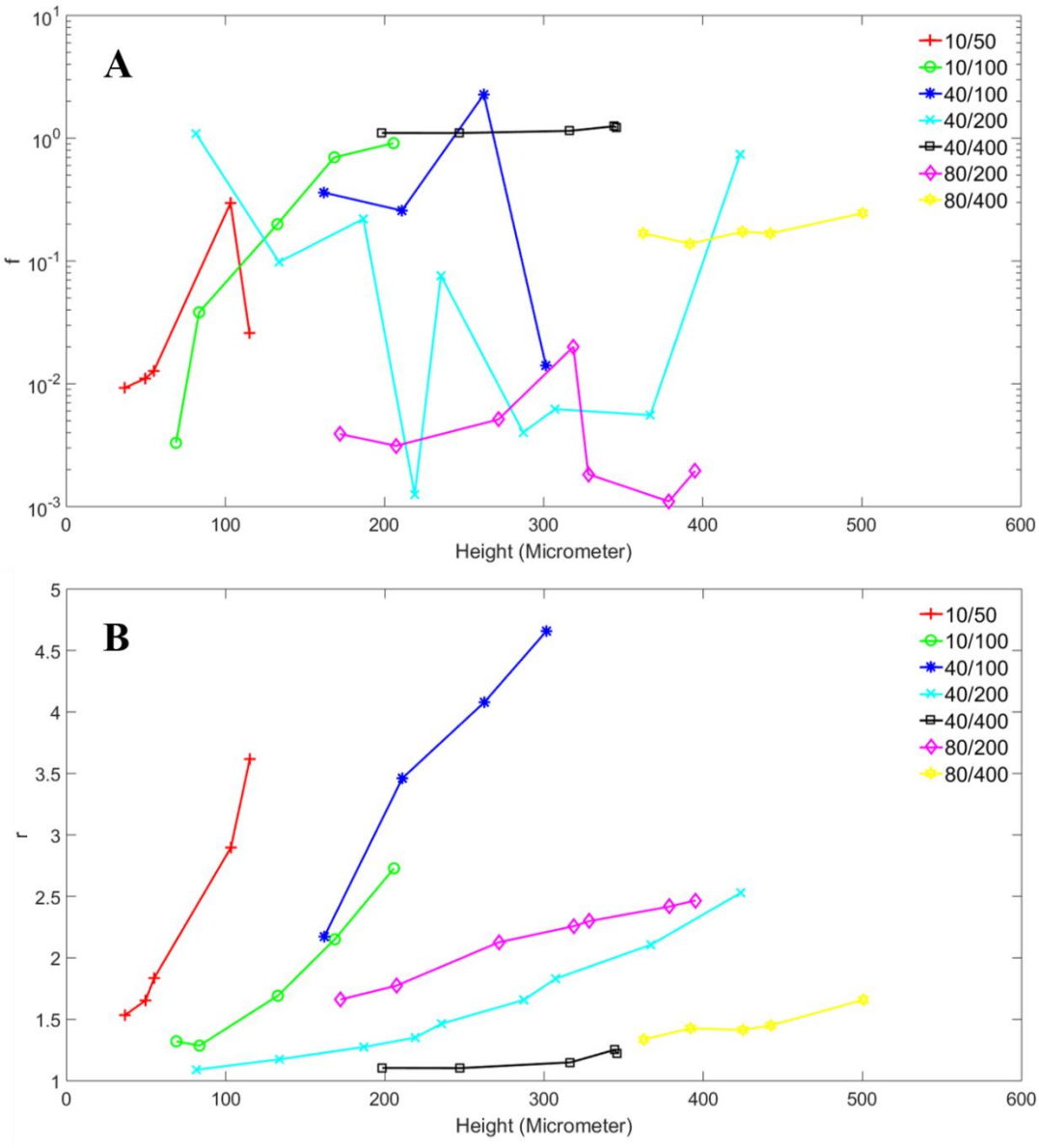

Figure 24 A: *f* versus mean height *H* and B: *f* versus *H*.

The *f* and *r* are being plotted versus *H* respectively in Figure 24. Logarithm axis was used for *f* for a better view, but the trends are only clear for 10/100, 40/400 and 80/400 samples. This is because of the error in observation and measurement of S_{Non} for *f* values being calculated. On the other hand, the roughness factor *r* shows good trends for all samples, since S_P values are closely approximated; as height increases, the surface area value ascends, and follows *r*.

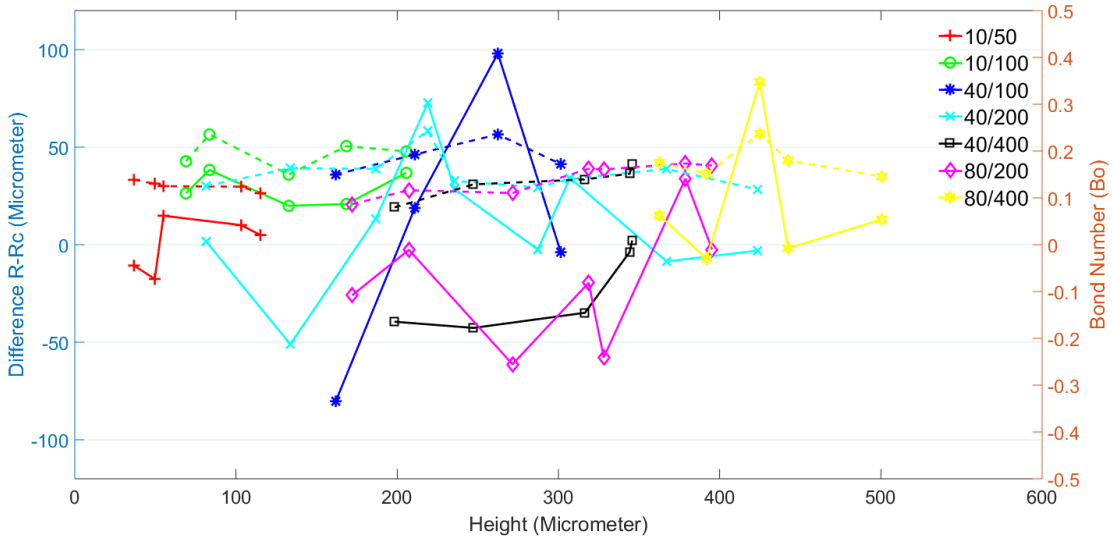

Figure 25 Droplet Radius Difference ΔR (Apex Fit radius R – Contact Fit radius R_C) and Bond Number versus Mean Structural Height. Bo values are shown in dashed lines.

The droplet shape is analyzed using both the Bond number and ΔR, the difference between apex radius (R) and contact fit radius (R_C). Utilizing the ImageJ software, R is fitted with multi-points and R_C is fitted with the plug-in. The Bond number is calculated from[58]

$$Bo = (\frac{l}{l_C})^2 \tag{12}$$

where l is the specific length and l_C is the capillary length of water, l_C =2.7 mm. In this case, l is equal to the apex radius R. In Figure 25, the Bond numbers are lower than 0.3, indicating that the droplets are mainly affected by surface tension. The negative values of ΔR show that the fitting circles for contact angle have larger radii than the apex circles, the equatorial radii are also greater, and the upper part of droplets are more closer to oblate spheroids; for positive ΔR, the upper part of droplets are closer to prolate spheroids . The relationship between droplet shape and actual contact angle is not significant, as shown in Figure 26.

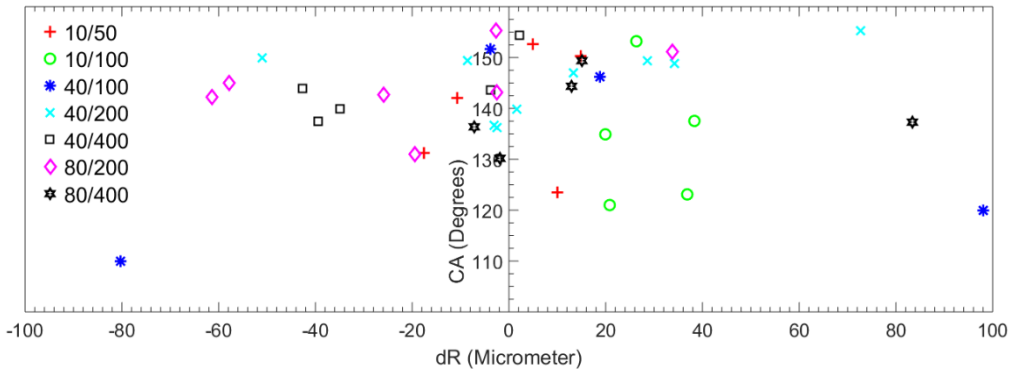

Figure 26 Scatter Plot of Contact Angle versus Δ*R*.

Among all the groups, 10/50, 10/100, and the 200-group samples perform high hydrophobicity within their specific range. The 80/200 sample with an initial thickness of 250 μm, mean actual height of 207.23 μm has the highest contact angle among all the samples. The samples are also translucent, as shown in Figure 27. The sample in the figure is the one with high hydrophobicity, and the two sides were cut for observation with the goniometer. Heterogeneity in all the samples was observed and is either due to the gradient in structural height or the bends on tips, or both. The edge is formed by the surface tension between the liquid feedstock and the cell wall, resulting in a higher thickness than at the center of the cell where the thickness is measured.

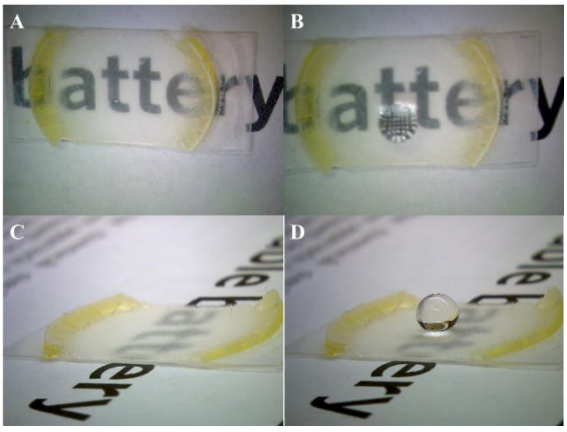

Figure 27 Transparency of a sample.

4 Conclusion

The process to produce superhydrophobic surfaces using a visible-light-inducted self-writing method has been achieved using photo-initiating compounds to cross-link the monomer. Total reflection inside the path way of light beams forms a pillar or cone-shaped microstructures with the aperture arrays on the photo mask. The performance of chemically coating PFDT was restricted by the system, and to enhance the performance, due to the refraction index, a light source of a different wavelength is needed, along with a photo-initiator working at the corresponding wavelength without affecting the reaction. Spraying of PTFE particles forms a smaller scale of microstructures on the surface of cones, which helps create strong hydrophobicity. The spacing and structural height have significant influences on the shape of the structure, thus affecting hydrophobicity; the coating materials are critical and the coating method is as well. A parameter set with less feedstock consumption was found. This method is fast, with 20 minutes of curing time for most spacing, 10 minutes for 80/200 and 400 spacing sets, and 10 minutes for the following procedures. The results have also demonstrated an approach to fabricate translucent superhydrophobic surfaces. Planned further work includes analyzing the hysteresis of the surface, finding out the relationship between droplet shape and the dimensional parameters.

References

1. Murphy, K. R., McClintic, W. T., Lester, K. C., Collier, C. P. & Boreyko, J. B. Dynamic Defrosting on Scalable Superhydrophobic Surfaces. *ACS Appl. Mater. Interfaces* **9,** 24308–24317 (2017).

2. Wang, Y., Xue, J., Wang, Q., Chen, Q. & Ding, J. Verification of Icephobic/Anti-icing Properties of a Superhydrophobic Surface. *ACS Appl. Mater. Interfaces* **5,** 3370–3381 (2013).

3. Zhou, C. *et al.* Nature-Inspired Strategy toward Superhydrophobic Fabrics for Versatile Oil/Water Separation. *ACS Appl. Mater. Interfaces* **9,** 9184–9194 (2017).

4. Liu, Q., Chen, D. & Kang, Z. One-Step Electrodeposition Process To Fabricate Corrosion-Resistant Superhydrophobic Surface on Magnesium Alloy. *ACS Appl. Mater. Interfaces* **7,** 1859–1867 (2015).

5. Xu, Q., Li, J., Tian, J., Zhu, J. & Gao, X. Energy-Effective Frost-Free Coatings Based on Superhydrophobic Aligned Nanocones. *ACS Appl. Mater. Interfaces* **6,** 8976–8980 (2014).

6. Kumar, D. *et al.* Hydrophobic sol–gel coatings based on polydimethylsiloxane for self-cleaning applications. *Mater. Des.* **86,** 855–862 (2015).

7. Cao, W.-T., Liu, Y.-J., Ma, M.-G. & Zhu, J.-F. Facile preparation of robust and superhydrophobic materials for self-cleaning and oil/water separation. *Colloids Surfaces A Physicochem. Eng. Asp.* **529,** 18–25 (2017).

8. Shen, L. *et al.* Asymmetric Free-Standing Film with Multifunctional Anti-Bacterial and Self-Cleaning Properties. *ACS Appl. Mater. Interfaces* **4,** 4476–4483 (2012).

9. Maeztu, J. D. *et al.* Effect of graphene oxide and fluorinated polymeric chains incorporated in a multilayered sol-gel nanocoating for the design of corrosion resistant and hydrophobic surfaces. *Appl. Surf. Sci.* **419,** 138–149 (2017).

10. Hong, S.-J., Chou, T.-H., Chan, S. H., Sheng, Y.-J. & Tsao, H.-K. Droplet Compression and Relaxation by a Superhydrophobic Surface: Contact Angle Hysteresis. *Langmuir* **28,** 5606–5613 (2012).

11. Cassie, A. B. D. & Baxter, S. Wettability of porous surfaces. *Trans. Faraday Soc.* **40,** 546 (1944).

12. Marmur, A. Wetting on hydrophobic rough surfaces: To be heterogeneous or not to be? *Langmuir* **19,** 8343–8348 (2003).

13. Young, T. An Essay on the Cohesion of Fluids. *Philos. Trans. R. Soc. London* **95,** 65–87 (1805).

14. Wenzel, R. N. RESISTANCE OF SOLID SURFACES TO WETTING BY WATER. *Ind. Eng. Chem.* **28,** 988–994 (1936).

15. Hejazi, V., Moghadam, A. D., Rohatgi, P. & Nosonovsky, M. Beyond Wenzel and Cassie–Baxter: Second-Order Effects on the Wetting of Rough Surfaces. *Langmuir* **30,** 9423–9429 (2014).

16. Xiang, M., Wilhelm, A. & Luo, C. Existence and Role of Large Micropillars on the Leaf Surfaces of *The President* Lotus. *Langmuir* **29,** 7715–7725 (2013).

17. Yang Yu, Zhi-Hua Zhao, and & Zheng*, Q.-S. Mechanical and Superhydrophobic Stabilities of Two-Scale Surfacial Structure of Lotus Leaves. (2007). doi:10.1021/LA7003485

18. Zhang, J., Sheng, X. & Jiang, L. The Dewetting Properties of Lotus Leaves. *Langmuir* **25,** 1371–1376 (2009).

19. Yamamoto, M. *et al.* Theoretical Explanation of the Lotus Effect: Superhydrophobic Property Changes by Removal of Nanostructures from the Surface of a Lotus Leaf. *Langmuir* **31,** 7355–7363 (2015).

20. Zhang, J. *et al.* How does the leaf margin make the lotus surface dry as the lotus leaf floats on water? *Soft Matter* **4,** 2232 (2008).

21. Li, M. *et al.* Hierarchically porous micro/nanostructured copper surfaces with enhanced antireflection and hydrophobicity. *Appl. Surf. Sci.* **361,** 11–17 (2016).

22. N. J. Shirtcliffe, *, G. McHale, M. I. Newton, and & Perry, C. C. Wetting and Wetting Transitions on Copper-Based Super-Hydrophobic Surfaces. (2005). doi:10.1021/LA048630S

23. Ruiz-Cabello, F. J. M. *et al.* Testing the performance of superhydrophobic aluminum surfaces. *J. Colloid Interface Sci.* **508,** 129–136 (2017).

24. Hermelin, E. *et al.* Ultrafast Electrosynthesis of High Hydrophobic Polypyrrole Coatings on a Zinc Electrode: Applications to the Protection against Corrosion. *Chem. Mater.* **20,** 4447–4456 (2008).

25. Pouget, E. *et al.* Well-Architectured Poly(dimethylsiloxane)-Containing Copolymers Obtained by Radical Chemistry. *Chem. Rev.* **110,** 1233–1277 (2010).

26. Park, E. J. *et al.* Hydrophobic Polydimethylsiloxane (PDMS) Coating of Mesoporous Silica and Its Use as a Preconcentrating Agent of Gas Analytes. *Langmuir* **30,** 10256–10262 (2014).

27. Lee, S. Y., Rahmawan, Y. & Yang, S. Transparent and Superamphiphobic Surfaces from Mushroom-Like Micropillar Arrays. *ACS Appl. Mater. Interfaces* **7,** 24197–24203 (2015).

28. Tropmann, A., Tanguy, L., Koltay, P., Zengerle, R. & Riegger, L. Completely Superhydrophobic PDMS Surfaces for Microfluidics. *Langmuir* **28,** 8292–8295 (2012).

29. Liu, H. *et al.* Robust translucent superhydrophobic PDMS/PMMA film by facile one-step spray for self-cleaning and efficient emulsion separation. *Chem. Eng. J.* **330,** 26–35 (2017).

30. Tom T. Huang, †,‡, David G. Taylor, ‡, Miroslav Sedlak, †, Nathan S. Mosier, †,§ and & Michael R. Ladisch†, §,⊥. Microfiber-Directed Boundary Flow in Press-Fit Microdevices Fabricated from Self-Adhesive Hydrophobic Surfaces. (2005). doi:10.1021/AC048228I

31. Huang, Y.-H., Wu, J.-T. & Yang, S.-Y. Direct fabricating patterns using stamping transfer process with PDMS mold of hydrophobic nanostructures on surface of micro-cavity. *Microelectron. Eng.* **88,** 849–854 (2011).

32. Zhang, L., Kwok, H., Li, X. & Yu, H.-Z. Superhydrophobic Substrates from Off-the-Shelf Laboratory Filter Paper: Simplified Preparation, Patterning, and Assay Application. *ACS Appl. Mater. Interfaces* **9,** 39728–39735 (2017).

33. Ogihara, H., Xie, J., Okagaki, J. & Saji, T. Simple Method for Preparing Superhydrophobic Paper: Spray-Deposited Hydrophobic Silica Nanoparticle Coatings Exhibit High Water-Repellency and Transparency. *Langmuir* **28,** 4605–4608 (2012).

34. Mayrhofer, L. *et al.* Fluorine-Terminated Diamond Surfaces as Dense Dipole Lattices: The Electrostatic Origin of Polar Hydrophobicity. *J. Am. Chem. Soc.* **138,** 4018–4028 (2016).

35. L. van Ravenstein, † *et al.* Low Surface Energy Polymeric Films from Novel Fluorinated Blocked Isocyanates. (2003). doi:10.1021/MA035296I

36. de Gennes, P. G. Wetting: statics and dynamics. *Rev. Mod. Phys.* **57,** 827–863 (1985).

37. Chhatre, S. S. *et al.* Fluoroalkylated Silicon-Containing Surfaces−Estimation of Solid-Surface Energy. *ACS Appl. Mater. Interfaces* **2,** 3544–3554 (2010).

38. Wang, L., Wei, J. & Su, Z. Fabrication of Surfaces with Extremely High Contact Angle Hysteresis from Polyelectrolyte Multilayer. *Langmuir* **27,** 15299–15304 (2011).

39. Zhang, H. *et al.* A stable 3D sol-gel network with dangling fluoroalkyl chains and rapid self-healing ability as a long-lived superhydrophobic fabric coating. *Chem. Eng. J.* **334,** 598–610 (2018).

40. Qiang, S., Chen, K., Yin, Y. & Wang, C. Robust UV-cured superhydrophobic cotton fabric surfaces with self-healing ability. *Mater. Des.* **116,** 395–402 (2017).

41. Gao, A., Liu, F., Xiong, Z. & Yang, Q. Tunable adhesion of superoleophilic/superhydrophobic poly (lactic acid) membrane for controlled-release of oil soluble drugs. *J. Colloid Interface Sci.* **505,** 49–58 (2017).

42. and, S. M. & Lee, H. J. Design of a Superhydrophobic Surface Using Woven Structures. (2007). doi:10.1021/LA063157Z

43. Cengiz, U. & Elif Cansoy, C. Applicability of Cassie–Baxter equation for superhydrophobic fluoropolymer–silica composite films. *Appl. Surf. Sci.* **335,** 99–106 (2015).

44. Zhan, Y. L. *et al.* Fabrication of anisotropic PTFE superhydrophobic surfaces using laser microprocessing and their self-cleaning and anti-icing behavior. *Colloids Surfaces A Physicochem. Eng. Asp.* **535,** 8–15 (2017).

45. Milionis, A. *et al.* Spatially Controlled Surface Energy Traps on Superhydrophobic Surfaces. *ACS Appl. Mater. Interfaces* **6,** 1036–1043 (2014).

46. Ganster, B., Fischer, U. K., Moszner, N. & Liska, R. New Photocleavable Structures. Diacylgermane-Based Photoinitiators for Visible Light Curing. *Macromolecules* **41,** 2394–2400 (2008).

47. Depew, M. C. & Wan, J. K. S. A time-resolved CIDEP study of the photogenerated camphorquinone radical anion: a case of dual singlet and triplet precursors. *J. Phys. Chem.* **90,** 6597–6600 (1986).

48. Crivello, J. V. A new visible light sensitive photoinitiator system for the cationic polymerization of epoxides. *J. Polym. Sci. Part A Polym. Chem.* **47,** 866–875 (2009).

49. Shi, S., Croutxé-Barghorn, C. & Allonas, X. Photoinitiating systems for cationic photopolymerization: Ongoing push toward long wavelengths and low light intensities. *Prog. Polym. Sci.* **65,** 1–41 (2017).

50. Chen, F. H., Pathreeker, S., Biria, S. & Hosein, I. D. Synthesis of Micropillar Arrays via Photopolymerization: An in Situ Study of Light-Induced Formation, Growth Kinetics, and the Influence of Oxygen Inhibition. *Macromolecules* **50,** 5767–5778 (2017).

51. Crivello, J. V. Redox initiated cationic polymerization. *J. Polym. Sci. Part A Polym. Chem.* **47,** 1825–1835 (2009).

52. Crivello, J. V. & Lam, J. H. W. Diaryliodonium Salts. A New Class of Photoinitiators for Cationic Polymerization. *Macromolecules* **10,** 1307–1315 (1977).

53. Fernández, A. *et al.* Design of Hierarchical Surfaces for Tuning Wetting Characteristics. *ACS Appl. Mater. Interfaces* **9,** 7701–7709 (2017).

54. Hatanaka, L. C., Wang, Q., Cheng, Z. & Mannan, M. S. Effect of trimethylolpropane triacrylate cross-linkages on the thermal stability and char yield of poly (methyl methacrylate) nanocomposites. *Fire Saf. J.* **87,** 65–70 (2017).

55. Crivello, J. V. & Reichmanis, E. Photopolymer Materials and Processes for Advanced Technologies. *Chem. Mater.* **26,** 533–548 (2014).

56. Yi, S.-L., Li, M.-C., Hu, X.-Q., Mo, W.-M. & Shen, Z.-L. An efficient and convenient method for the preparation of disulfides from thiols using oxygen as oxidant catalyzed by tert-butyl nitrite. *Chinese Chem. Lett.* **27,** 1505–1508 (2016).

57. Ishino, C. & Okumura, K. Wetting transitions on textured hydrophilic surfaces. *Eur. Phys. J. E* **25,** 415–424 (2008).

58. Liu, T. 'Leo' & Kim, C.-J. 'CJ'. Contact Angle Measurement of Small Capillary Length Liquid in Super-repelled State. *Sci. Rep.* **7,** 740 (2017).

Vita

Hansheng Li had achieved the bachelor degree in applied chemistry at Sichuan University in 2014 and started the chemical engineering program for masters' degree at Syracuse University in 2015. The research in this thesis started in fall 2016.